REPORT DOCUMENTATION PAGE

Form Approved
OMB No. 0704-0188

1. REPORT DATE *(DD-MM-YYYY)*	2. REPORT TYPE	3. DATES COVERED *(From - To)*
21-12-2011	Conference Paper	

4. TITLE AND SUBTITLE

Investigation of Nonequilibrium Effects in Axisymmetric Nozzle and Blunt Body Nitrogen Flows by Means of a Reduced Rovibrational Collisional Model

5a. CONTRACT NUMBER

5b. GRANT NUMBER

5c. PROGRAM ELEMENT NUMBER

6. AUTHOR(S)

Alessandro Munafò, Michael G. Kapper, Jean-Luc Cambier, and Thierry E. Magin

5d. PROJECT NUMBER

5f. WORK UNIT NUMBER
23041057

7. PERFORMING ORGANIZATION NAME(S) AND ADDRESS(ES)

Air Force Research Laboratory (AFMC)
AFRL/RZSS
1 Ara Drive
Edwards AFB CA 93524-7013

8. PERFORMING ORGANIZATION REPORT NUMBER

9. SPONSORING / MONITORING AGENCY NAME(S) AND ADDRESS(ES)

Air Force Research Laboratory (AFMC)
AFRL/RZS
5 Pollux Drive
Edwards AFB CA 93524-7048

10. SPONSOR/MONITOR'S ACRONYM(S)

11. SPONSOR/MONITOR'S NUMBER(S)
AFRL-RZ-ED-TP-2011-585

12. DISTRIBUTION / AVAILABILITY STATEMENT

Distribution A: Approved for public release; distribution unlimited. PA# 12029.

13. SUPPLEMENTARY NOTES

For presentation at the 50th AIAA Aerospace Sciences Meeting, Nashville, TN, 9-12 Jan 2012.

14. ABSTRACT

A vibrational collisional model is proposed to study the internal energy excitation and dissociation processes in 2D axisymmetric nonequilibrium nitrogen flows. The chemical database for theN+N2 system recently developed at NASA Ames Research Center provides rate coefficients for rovibrational dissociation and excitation. Vibrationally averaged rate coefficients for N +N2 inelastic collisions are computed based on the hypothesis of equilibrium between translational and rotational modes. Inelastic N2 +N2 collisions are also considered based on literature data. The governing equations for 2D inviscid axisymmetric nonequilibrium flows are discretized in space by means of the finite volume method. Time integration is performed through the use of the operator splitting approach. Applications to the supersonic flow through the converging-diverging nozzle of the NASA Ames EAST (Electric Arc Shock Tube) facility and to the flow over a sphere, show that populations of vibrational levels experience departure from a Boltzmann distribution. For the nozzle case, experimental data are available and have been compared against computational results. A good agreement between the two is observed.

15. SUBJECT TERMS

16. SECURITY CLASSIFICATION OF:			17. LIMITATION OF ABSTRACT	18. NUMBER OF PAGES	19a. NAME OF RESPONSIBLE PERSON
					Dr. Jean-Luc Cambier
a. REPORT	b. ABSTRACT	c. THIS PAGE	SAR	18	19b. TELEPHONE NUMBER *(include area code)*
Unclassified	**Unclassified**	**Unclassified**			N/A

Investigation of Nonequilibrium Effects in Axisymmetric Nozzle and Blunt Body Nitrogen Flows by means of a Reduced Rovibrational Collisional Model

Alessandro Munafò*
von Karman Institute for Fluid Dynamics, Belgium
Michael G. Kapper†
von Karman Institute for Fluid Dynamics, Belgium
Jean-Luc Cambier‡
Edwards Air Force Research Laboratory, USA
Thierry E. Magin§
von Karman Institute for Fluid Dynamics, Belgium

A vibrational collisional model is proposed to study the internal energy excitation and dissociation processes in 2D axisymmetric nonequilibrium nitrogen flows. The chemical database for the $N + N_2$ system recently developed at NASA Ames Research Center provides rate coefficients for rovibrational dissociation and excitation. Vibrationally averaged rate coefficients for $N + N_2$ inelastic collisions are computed based on the hypothesis of equilibrium between translational and rotational modes. Inelastic $N_2 + N_2$ collisions are also considered based on literature data. The governing equations for 2D inviscid axisymmetric nonequilibrium flows are discretized in space by means of the finite volume method. Time integration is performed through the use of the operator splitting approach. Applications to the supersonic flow through the converging-diverging nozzle of the NASA Ames EAST (Electric Arc Shock Tube) facility and to the flow over a sphere, show that populations of vibrational levels experience departure from a Boltzmann distribution. For the nozzle case, experimental data are available and have been compared against computational results. A good agreement between the two is observed.

*PhD. candidate, Aeronautics/Aerospace department, von Karman Institute for Fluid Dynamics, Chaussée de Waterloo 72, 1640 Rhode-Saint-Genèse, Belgium, AIAA member.
†Post doctoral fellow, Aeronautics/Aerospace department, von Karman Institute for Fluid Dynamics, Chaussée de Waterloo 72, 1640 Rhode-Saint-Genèse, Belgium.
‡Senior research scientist, Air Force Research Laboratory, 10 E. Saturn Blvd., Edwards Air Force Research Laboratory, CA 93524, USA
§Assistant professor, Aeronautics/Aerospace department, von Karman Institute for fluid dynamics, Chaussée de Waterloo 72, 1640 Rhode-Saint-Genèse, Belgium, AIAA member.

Nomenclature

F	inviscid flux vector (axial direction)
G	inviscid flux vector (radial direction)
K	right eigenvector matrix
L	left eigenvector matrix
R	right-hand-side residual vector
S	source term vector
U	conservative variable vector
A	nozzle cross sectional area
a	frozen speed of sound
b	upwind wave speed
E	energy or specific total energy
e	specific energy
g	degeneracy
H	specific total enthalpy
h	specific enthalpy
i	axial direction cell index
J	rotational quantum number
j	radial direction cell index
k	rate coefficient
l	cell side length
M	molecular mass
m	mass
p	pressure
Q	partition function
R	specific gas constant
r	radial coordinate
T	temperature
t	time
u	velocity component
v, w	vibrational quantum number
x	axial coordinate

Subscripts

$*$	dissociated state
∞	free-stream value
b	backward
f	forward
J	rotational quantum number
L	left state
n	cell side outward normal direction
R	right state
r	radial direction
v, w	vibrational quantum number
x	axial direction

Conventions

c	convection
D	dissociation
s	source
VT	vibrational-translational energy exchange
VV	vibrational-vibrational energy exchange

Symbols

α	parameter used in the reconstruction procedure

Δ variation
δ variation
$\mathbf{\Lambda}$ eigenvalue matrix
Ω cell volume
ρ density
σ symmetry factor
θ characteristic rotational temperature

Superscripts

a atomic impact process
axi axisymmetric
chem chemistry
m molecular impact process
v vibration
f formation
n time-level
t translation

I. Introduction

Possible applications of atmospheric entry flows are the design of space vehicle heat shields and interpretation of experimental data acquired in high enthalpy facilities, such as shock tunnels and plasma torches. The surface heat flux experienced by a spacecraft during his re-entry represents the main design parameter. Its value must be accurately predicted in order to avoid mission failure and also to reduce the margins to enable carrying more payload. In order to achieve this point, an accurate modeling of collisional and radiative processes occurring in shock layers is needed. There, the flow experiences a sudden increase of temperature, pressure and density while crossing the shock wave. Atom and molecule collisions start occurring at higher frequencies and energies. This leads to excitation of internal degrees of freedom and to molecular dissociation as well. If the re-entry speed is high enough, ionization may also occur. The flow becomes therefore a partially ionized gas, where radiative transitions take place. Their influence on the medium dynamics and surface heat flux increases with the increase of the entry speed. As an example, for an Earth re-entry at 11 km/s, the radiative heat flux constitutes approximately 60% of the total heating. The accurate description of all these phenomena is extremely complex because of nonequilibrium. This occurs in flow regions (such as shock waves and boundary layers) where the characteristic time-scales of collisional and radiative processes become of the same order of magnitude of flow macroscopic time-scales (time needed for a fluid particle to cross a certain region). Therefore, understanding nonequilibrium is crucial for a correct modeling of shock layers. Nonequilibrium plays an important role also in expanding flows, such as those occurring in nozzles installed in high enthalpy facilities. When heat flux and pressure measurements are performed on the model being tested, it is required to know the degree of nonequilibrium in the free-stream (generated by the nozzle) if an extrapolation to flight of ground testing data is desired.

Multi-temperature models [1] were proposed as a simple approach to overcome all difficulties related to the modeling of nonequilibrium. They are based on Boltzmann distributions of the internal energy levels at their own temperatures and are valid only in case of small departure from equilibrium [2], since the details of energy level dynamics are not taken into account. These models are widely used outside of their range of validity because of the lack of more accurate physical models, but also because of the ease of implementation and reasonable amount of CPU time required for 3D simulations.

State-to-state or collisional models [3–15], in contrast to the multi-temperature formulation, treat each energy level as a separated pseudo-species. This approach provides more flexibility and accuracy, since effects of non-Boltzmann distributions are accounted for. The price to pay is that a very large number of processes have to be considered and, for each one, rate coefficient values have to be obtained by means of quantum-mechanical calculations. Also, the number of equations to be solved rapidly increases with the number of internal energy levels.

The main purpose of the paper is to show that, despite the higher computational time required, the application of collisional models to multi-dimensional nonequilibrium flows has become feasible. The results shown represent the outcome of on going research activity and are limited to inviscid flows.

The paper is structured as follows. Sect. II describes the physical model adopted (collisional processes,

rate coefficient expressions and governing equations in conservation law form). The numerical method is outlined in Sect. III. Computational results are discussed in Sect. IV. Conclusions are given in Sect. V.

II. Physical modeling

It is assumed that the flow conditions are such that the translational and rotational degrees of freedom of molecules are in equilibrium. This hypothesis is not always verified across shock waves [2], while it holds, in general, for an expansion through a converging-diverging nozzle in view of the fast and efficient energy exchange between rotation and translation at temperatures and pressures typical of nozzles installed in high enthalpy wind tunnels.

Chemical database

The starting point for the development of the vibrational collisional (VC) model in use is the chemical database recently developed at NASA Ames Research Center [3–6], providing rate coefficients for the following processes involving the rovibrational levels of the nitrogen molecule in its ground electronic state:

- Rovibrational dissociation:

$$\mathrm{N_2}(v,J)+\mathrm{N} \underset{k^{\mathrm{a}}_{b\,vJ\to *}}{\overset{k^{\mathrm{a}}_{f\,vJ\to *}}{\rightleftharpoons}} \mathrm{N}+\mathrm{N}+\mathrm{N}, \tag{1}$$

- Rovibrational excitation:

$$\mathrm{N_2}(v,J)+\mathrm{N} \underset{k^{\mathrm{a}}_{b\,vJ\to v'J'}}{\overset{k^{\mathrm{a}}_{f\,vJ\to v'J'}}{\rightleftharpoons}} \mathrm{N_2}(v',J')+\mathrm{N}, \tag{2}$$

with $v=0,\ldots,v_{\max}$, $v'>v$, $J=0,\ldots,J_{\max}(v)$ and $J'=0,\ldots,J_{\max}(v')$. Rate coefficients for rovibrational dissociation and excitation are computed by means of the quasi-classical trajectory (QCT) method after generating realistic nuclear interaction potentials by means of quantum-mechanics. Their values are available within the range $7500-50000\,\mathrm{K}$ (see [3–6] for more details).

The energy of a rovibrational level vJ is written as:

$$E_{vJ}=\tilde{E}_v+\Delta E_{vJ} \tag{3}$$

where $\tilde{E}_v=E_{v0}$ is the vibrational energy and $\Delta E_{vJ}=E_{vJ}-\tilde{E}_v$ is the rotational energy. The splitting in eq. (3) is not unique and other choices are possible [16].

Fig. 1 shows the energy and energy spacing as function of the vibrational quantum number. Anharmonicity effects can be noticed starting from low quantum states.

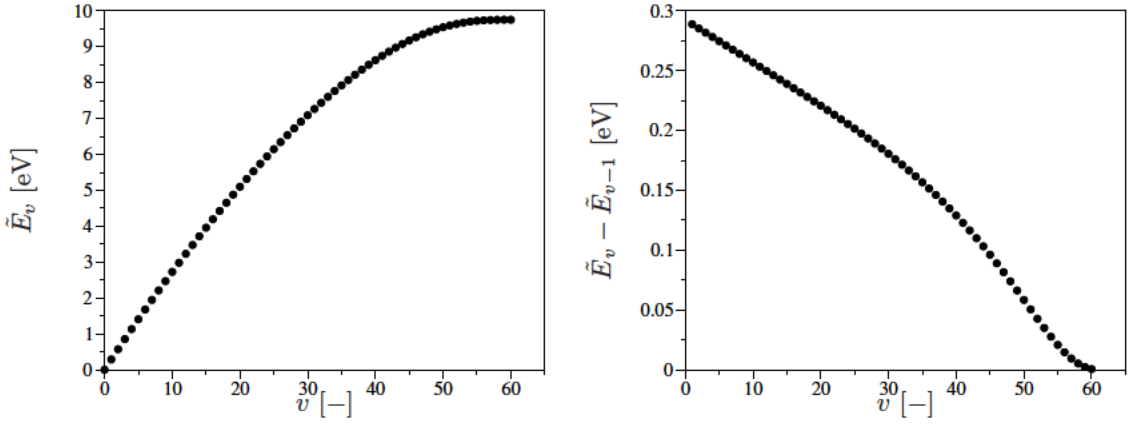

(a) Energy. (b) Energy spacing.

Figure 1. Vibrational energy levels and spacings.

Vibrational collisional model

The VC model accounts for the following processes:

- Atomic impact dissociation ($\mathrm{D_a}$):

$$\mathrm{N_2}(v) + \mathrm{N} \underset{\tilde{k}^{\mathrm{a}}_{b\,v\to *}}{\overset{\tilde{k}^{\mathrm{a}}_{f\,v\to *}}{\rightleftharpoons}} \mathrm{N} + \mathrm{N} + \mathrm{N}, \tag{4}$$

- Molecular impact dissociation ($\mathrm{D_m}$):

$$\mathrm{N_2}(v) + \mathrm{N_2} \underset{\tilde{k}^{\mathrm{m}}_{b\,v\to *}}{\overset{\tilde{k}^{\mathrm{m}}_{f\,v\to *}}{\rightleftharpoons}} \mathrm{N} + \mathrm{N} + \mathrm{N_2}, \tag{5}$$

- Atomic impact vibrational-translational energy exchange ($\mathrm{VT_a}$):

$$\mathrm{N_2}(v) + \mathrm{N} \underset{\tilde{k}^{\mathrm{a}}_{b\,v\to v'}}{\overset{\tilde{k}^{\mathrm{a}}_{f\,v\to v'}}{\rightleftharpoons}} \mathrm{N_2}(v') + \mathrm{N}, \tag{6}$$

- Molecular impact vibrational-translational energy exchange ($\mathrm{VT_m}$):

$$\mathrm{N_2}(v) + \mathrm{N_2} \underset{\tilde{k}^{\mathrm{m}}_{b\,v\to v-1}}{\overset{\tilde{k}^{\mathrm{m}}_{f\,v\to v-1}}{\rightleftharpoons}} \mathrm{N_2} + \mathrm{N_2}(v-1), \tag{7}$$

- Vibrational-vibrational energy exchange (VV):

$$\mathrm{N_2}(v) + \mathrm{N_2}(w-1) \underset{\tilde{k}_{b\,v\to v-1}^{\,w-1\to w}}{\overset{\tilde{k}_{f\,v\to v-1}^{\,w-1\to w}}{\rightleftharpoons}} \mathrm{N_2}(v-1) + \mathrm{N_2}(w), \tag{8}$$

with $v = 0, \ldots, v_{\max}$ (except for eq. (8) where $v = 1, \ldots, v_{\max}$), $v' = v+1, \ldots, v_{\max}$ and $w = v, \ldots, v_{\max}$.

Rate coefficients and species production rates

Forward rate coefficients for $\mathrm{D_a}$ and $\mathrm{VT_a}$ processes in eqs. (4) and (6) are obtained by averaging rovibrational rate coefficients for dissociation and excitation ($k^{\mathrm{a}}_{f\,vJ\to *}$ and $k^{\mathrm{a}}_{f\,vJ\to v'J'}$, respectively) over a Boltzmann distribution for rotational levels of each vibrational quantum state [17]:

$$\tilde{k}^{\mathrm{a}}_{f\,v\to *} = \frac{1}{\tilde{Q}_v} \sum_{J=0}^{J_{\max}(v)} g_{vJ} \exp\left(-\frac{\Delta E_{vJ}}{k_{\mathrm{B}} T}\right) k^{\mathrm{a}}_{f\,vJ\to *}, \tag{9}$$

$$\tilde{k}^{\mathrm{a}}_{f\,v\to v'} = \frac{1}{\tilde{Q}_v} \sum_{J=0}^{J_{\max}(v)} g_{vJ} \exp\left(-\frac{\Delta E_{vJ}}{k_{\mathrm{B}} T}\right) \sum_{J'=0}^{J_{\max}(v')} k^{\mathrm{a}}_{f\,vJ\to v'J'}, \quad v = 0, \ldots, v_{\max}, \quad v < v' \tag{10}$$

where k_{B} is the Boltzmann constant, g_{vJ} is the energy level degeneracy (equal to $6\,(J+1)$ for even J and $3\,(J+1)$ for odd J) and $\tilde{Q}_v$ is the rotational partition function of the vibrational level v [17]:

$$\tilde{Q}_v = \sum_{J=0}^{J_{\max}(v)} g_{vJ} \exp\left(-\frac{\Delta E_{vJ}}{k_{\mathrm{B}} T}\right) \tag{11}$$

Backward rate coefficients are computed by means of micro-reversibility [17]:

$$\frac{\tilde{k}^{\mathrm{a}}_{b\,v\to *}}{\tilde{k}^{\mathrm{a}}_{f\,v\to *}} = \frac{Q^t_{\mathrm{N_2}} \tilde{Q}_v}{(g_{\mathrm{N}}\, Q^t_{\mathrm{N}})^2} \exp\left(-\frac{\tilde{E}_v - 2E_{\mathrm{N}}}{k_{\mathrm{B}} T}\right), \tag{12}$$

$$\frac{\tilde{k}^{\mathrm{a}}_{b\,v\to v'}}{\tilde{k}^{\mathrm{a}}_{f\,v\to v'}} = \frac{\tilde{Q}_v}{\tilde{Q}_{v'}} \exp\left(-\frac{\tilde{E}_v - \tilde{E}_{v'}}{k_{\mathrm{B}} T}\right), \quad v = 0, \ldots, v_{\max} \tag{13}$$

where $E_{\rm N}$ is the formation energy of the nitrogen atom, $g_{\rm N} = 12$ the degeneracy of its ground electronic state (N ^{4}S nuclear and electronic spin contributions) and $Q^t_{\rm N}$ and $Q^t_{\rm N_2}$ are the translational partition functions of the N atom and N_2 molecule, respectively:

$$Q^t_{\rm N} = \left(\frac{2\pi m_{\rm N} k_{\rm B} T}{h_{\rm P}^2}\right)^{3/2}, \quad Q^t_{\rm N_2} = \left(\frac{2\pi m_{\rm N_2} k_{\rm B} T}{h_{\rm P}^2}\right)^{3/2} \tag{14}$$

where $h_{\rm P}$ is the Planck constant.

Rate coefficients for $N_2 + N_2$ inelastic collisions are not available in the NASA Ames database. It is for this reason that data from literature are considered for $\rm D_m$, $\rm VT_m$ and VV processes.

The estimation of rate coefficients for the $\rm D_m$ process is performed by multi-plying $\tilde{k}^{\rm a}_{b\,v\to *}$ in eq. (9) by the Park factor $f_{\rm Park} = 0.23$ [18]:

$$\tilde{k}^{\rm m}_{f\;v\to *} = f_{\rm Park}\, \tilde{k}^{\rm a}_{f\,v\to *} \tag{15}$$

while the backward rate coefficient is obtained by means of micro-reversibility:

$$\frac{\tilde{k}^{\rm m}_{b\;v\to *}}{\tilde{k}^{\rm m}_{f\;v\to *}} = \frac{Q^t_{\rm N_2}\tilde{Q}_v}{(g_{\rm N}\, Q^t_{\rm N})^2} \exp\left(-\frac{\tilde{E}_v - 2E_{\rm N}}{k_{\rm B}T}\right) \tag{16}$$

Though not rigorous, this approach allows to take into account that N_2 is a less effective collision partner than N for dissociation.

The computation of forward rate coefficients for $\rm VT_m$ and VV processes is performed by adapting the existing set of Billing data [19] (based on Herzberg [20] vibrational energy levels) to the vibrational levels of the NASA Ames database. The procedure is similar to that in [21] and makes use of the so called scaling laws taking into account for anharmonicity effects [22]. Backward rate coefficients are always obtained by means of micro-reversibility:

$$\frac{\tilde{k}^{\rm m}_{b\;v\to v-1}}{\tilde{k}^{\rm m}_{f\;v\to v-1}} = \frac{\tilde{Q}_v}{\tilde{Q}_{v-1}} \exp\left(-\frac{\tilde{E}_v - \tilde{E}_{v-1}}{k_{\rm B}T}\right), \tag{17}$$

$$\frac{\tilde{k}_b{}^{w-1\to w}_{v\to v-1}}{\tilde{k}_f{}^{w-1\to w}_{v\to v-1}} = \frac{\tilde{Q}_v\,\tilde{Q}_{w-1}}{\tilde{Q}_{v-1}\,\tilde{Q}_w} \exp\left(-\frac{\tilde{E}_v + \tilde{E}_{w-1} - \tilde{E}_{v-1} - \tilde{E}_w}{k_{\rm B}T}\right), \quad v = 1,\ldots,v_{\max}, \quad w \geq v \tag{18}$$

The species production rates for the N atom and vibrational levels of N_2 read:

$$\omega_{\rm N} = 2M_{\rm N}\sum_{v=0}^{v_{\max}} \tilde{\omega}_v^{\rm D_a} + 2M_{\rm N}\sum_{v=0}^{v_{\max}} \tilde{\omega}_v^{\rm D_m}, \tag{19}$$

$$\tilde{\omega}_v = -M_{\rm N_2}\left(\tilde{\omega}_v^{\rm D_a} + \tilde{\omega}_v^{\rm D_m} + \tilde{\omega}_v^{\rm VT_a} + \tilde{\omega}_v^{\rm VT_m} + \tilde{\omega}_v^{\rm VV}\right) \tag{20}$$

with the partial contributions from all processes given by:

$$\tilde{\omega}_v^{\rm D_a} = [X_{\rm N}]\left([\tilde{X}_v]\,\tilde{k}^{\rm a}_{f\,v\to *} - [X_{\rm N}]^2\,\tilde{k}^{\rm a}_{b\,v\to *}\right), \tag{21}$$

$$\tilde{\omega}_v^{\rm D_m} = [X_{\rm N_2}]\left([\tilde{X}_v]\,\tilde{k}^{\rm m}_{f\;v\to *} - [X_{\rm N}]^2\,\tilde{k}^{\rm m}_{b\;v\to *}\right), \tag{22}$$

$$\tilde{\omega}_v^{\rm VT_a} = [X_{\rm N}]\left([\tilde{X}_v]\,\tilde{k}^{\rm a}_{f\,v\to v'} - [\tilde{X}_{v'}]\,\tilde{k}^{\rm a}_{b\,v\to v'}\right), \tag{23}$$

$$\tilde{\omega}_v^{\rm VT_m} = [X_{\rm N_2}]\left([\tilde{X}_v]\,\tilde{k}^{\rm m}_{f\;v\to v-1} - [\tilde{X}_{v'}]\,\tilde{k}^{\rm m}_{b\;v\to v-1}\right) \tag{24}$$

$$\tilde{\omega}_v^{\rm VV} = \sum_{w=v}^{v_{\max}}\left([\tilde{X}_v]\,[\tilde{X}_{w-1}]\,\tilde{k}_f{}^{w-1\to w}_{v\to v-1} + [\tilde{X}_{v-1}]\,[\tilde{X}_w]\,\tilde{k}_b{}^{w-1\to w}_{v\to v-1}\right), \quad v = 0,\ldots,v_{\max} \tag{25}$$

where $[X_{\rm N}] = \rho_{\rm N}/M_{\rm N}$ and $[\tilde{X}_v] = \tilde{\rho}_v/M_{\rm N_2}$ are the concentrations of the N atom and N_2 vibrational levels, respectively.

Thermodynamics

The mixture density is obtained by adding the contributions from the N atom and N_2 vibrational levels $\rho = \rho_N + \rho_{N_2}$, where:

$$\rho_{N_2} = \sum_{v=0}^{v_{max}} \tilde{\rho}_v \tag{26}$$

and the static pressure follows from Dalton's law $p = \rho_N R_N T + \rho_{N_2} R_{N_2} T$ (where R_N and R_{N_2} are the specific gas constants). The mixture total energy density is computed as:

$$\rho E = \frac{3}{2}\rho_N R_N T + \frac{3}{2}\rho_{N_2} R_{N_2} T + \sum_{v=0}^{v_{max}} \tilde{\rho}_v(\tilde{e}_v + \Delta e_v) + \rho_N h_N^f + \frac{1}{2}\rho\left(u_x^2 + u_r^2\right) \tag{27}$$

where u_x and u_r are, respectively, the axial and radial velocity components, h_N^f is the specific formation enthalpy of the nitrogen atom and $\tilde{e}_v$ and Δe_v are, respectively, the specific vibrational and rotational energy of the vibrational level v:

$$\tilde{e}_v = \frac{\tilde{E}_v}{m_{N_2}}, \quad \Delta e_v(T) = \frac{k_B T^2}{m_{N_2}} \frac{\partial \ln \tilde{Q}_v}{\partial T}, \quad v = 0, \ldots, v_{max} \tag{28}$$

The mixture total enthalpy density ρH is obtained by adding the pressure to the total energy density.

In order to simplify computations, the rigid rotor model is used in eqs. (12), (13), (16), (18) and (28) for $\tilde{Q}_v$ and Δe_v. In this case one has:

$$\tilde{Q}_v = \frac{T}{\sigma \theta_r} \quad , \quad \Delta e_v = R_{N_2} T, \quad v = 0, \ldots, v_{max} \tag{29}$$

where σ is the symmetry factor (equal to 2 for a homo-nuclear diatomic molecule such as N_2), while θ_r is the characteristic rotational temperature (computed from the rovibrational energy levels as $(E_{01} - E_{00})/k_B$). The atomic nitrogen degeneracy g_N in eq. (12), must be modified accordingly and set to 4.

Preliminary computations performed on quasi 1D nozzle and normal shock wave flows, have allowed to verify that the aforementioned simplification could be applied for the cases under investigation.

Governing equations

The governing equations for 2D axisymmetric inviscid nonequilibrium flows, written in conservation law form, read:

$$\frac{\partial r\mathbf{U}}{\partial t} + \frac{\partial r\mathbf{F}}{\partial x} + \frac{\partial r\mathbf{G}}{\partial r} = \mathbf{S} \tag{30}$$

where $\mathbf{U}$, $\mathbf{F}$ and $\mathbf{G}$ are, respectively, the conservative variable vector and the inviscid flux vectors along the axial and radial directions. Their expressions are given by:

$$\mathbf{U} = \left[\ \rho_N \quad \tilde{\rho}_v \quad \rho u_x \quad \rho u_r \quad \rho E\ \right]^T, \tag{31}$$

$$\mathbf{F} = \left[\ \rho_N u_x \quad \tilde{\rho}_v u_x \quad p + \rho u_x^2 \quad \rho u_x u_r \quad \rho u_x H\ \right]^T, \tag{32}$$

$$\mathbf{G} = \left[\ \rho_N u_r \quad \tilde{\rho}_v u_r \quad \rho u_x u_r \quad p + \rho u_r^2 \quad \rho u_r H\ \right]^T, \quad v = 0, \ldots, v_{max} \tag{33}$$

The source term $\mathbf{S}$ in eq. (30) comprises the effects of the collisional processes previously described and an additional contribution due to the hypothesis of axisymmetric flow configuration:

$$\mathbf{S} = \mathbf{S}^{chem} + \mathbf{S}^{axi} \tag{34}$$

with the chemistry $\mathbf{S}^{chem}$ and axisymmetric $\mathbf{S}^{axi}$ terms in eq. (34) given by:

$$\mathbf{S}^{chem} = \left[\ r\,\omega_N \quad r\,\tilde{\omega}_v \quad 0 \quad 0 \quad 0\ \right]^T, \quad v = 0, \ldots, v_{max}, \tag{35}$$

$$\mathbf{S}^{axi} = \left[\ 0 \quad 0 \quad 0 \quad p \quad 0\ \right]^T \tag{36}$$

III. Numerical method

Numerical solutions to eq. (30) are obtained by means of a 2D multi-block parallel Finite Volume code developed for the application of collisional-radiative models to nonequilibrium flows [23–25].

Governing equations are discretized in space by means of the Finite Volume Method. This leads to the following semi-discrete equation for the cell i, j (see Fig. 2) conservative variable vector:

$$\Omega_{i,j} \frac{\partial \mathbf{U}_{i,j}}{\partial t} = -\mathbf{R}_{i,j} \tag{37}$$

where $\Omega_{i,j}$ is the cell volume and $\mathbf{R}_{i,j}$ is the right-hand-side residual made up convective and source term contributions:

$$\mathbf{R}_{i,j} = \mathbf{R}_{\mathrm{c}\,i,j} + \mathbf{R}_{\mathrm{s}\,i,j} \tag{38}$$

with:

$$\mathbf{R}_{\mathrm{c}\,i,j} = \tilde{\mathbf{F}}_{n\,i+\frac{1}{2},j}\, l_{i+\frac{1}{2},j} + \tilde{\mathbf{F}}_{n\,i-\frac{1}{2},j}\, l_{i-\frac{1}{2},j} + \tilde{\mathbf{F}}_{n\,i,j+\frac{1}{2}}\, l_{i,j+\frac{1}{2}} + \tilde{\mathbf{F}}_{n\,i,j-\frac{1}{2}}\, l_{i,j-\frac{1}{2}} \tag{39}$$

$$\mathbf{R}_{\mathrm{s}\,i,j} = -\mathbf{S}_{i,j}\Omega_{i,j} \tag{40}$$

In eq. (39), the tilde symbol ($\tilde{\cdot}$) indicates that a numerical flux function is used for the evaluation of convective fluxes at cell interfaces whose lengths are indicated by l (indices in eqs. (39) - (40) refer to Fig. 2).

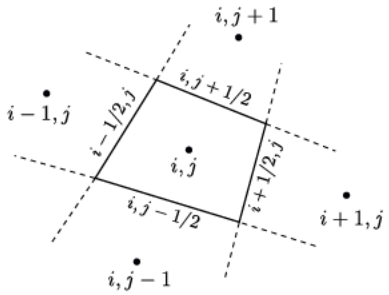

Figure 2. Sketch of cell ordering for the 2D structured grid code in use.

Once the right-hand-side residual split realized, the solution vector within the cell i, j is updated at its new value at time level $n + 1$ by adding contributions from the convection and source term steps:

$$\mathbf{U}^{n+1}_{i,j} = \mathbf{U}^{n}_{i,j} + \delta_{\mathrm{c}}\mathbf{U}^{n}_{i,j} + \delta_{\mathrm{s}}\mathbf{U}^{n}_{i,j} \tag{41}$$

In eq. (41), the two contributions to the solution update are computed independently as follows. During the convection step, the presence of source terms is neglected and the solution update is computed explicitly according to:

$$\delta_c\mathbf{U}^{n}_{i,j} = -\frac{\Delta t_{\mathrm{c}\,i,j}}{\Omega_{i,j}}\mathbf{R}^{n}_{\mathrm{c}\,i,j} \tag{42}$$

The convective time-step $\Delta t_{\mathrm{c}\,i,j}$ in eq. (42) is computed by means of the usual CFL-like condition [26] by imposing for each cell the maximum allowable time-step allowing for local stability (local time-stepping).

Once this done, the source term step is performed by neglecting flux contributions. Due to the stiffness associated to the source term, the solution update is performed by treating it implicitly:

$$\delta_s\mathbf{U}^{n}_{i,j} = \left(\frac{\mathbf{I}}{\Delta t_{\mathrm{s}\,i,j}} - \mathbf{J}^{n}_{i,j}\right)^{-1} \mathbf{S}^{n}_{i,j} \tag{43}$$

where $\mathbf{J} = \partial\mathbf{S}/\partial\mathbf{U}$ in eq. (43), is the source term Jacobian matrix. In order to enhance stability and reduce CPU time, the aforementioned quantity is computed analytically. The source time-step $\Delta t_{\mathrm{s}\,i,j}$ in eq. (43) should be computed from stability considerations on the ODE system $\partial\mathbf{U}/\partial t = \mathbf{S}$, and not from the CFL number. However, in the present work the simplifying assumption $\Delta t_{\mathrm{s}\,i,j} = \Delta t_{\mathrm{c}\,i,j}$ was adopted, since for the cases under investigation it did not lead to a too severe restriction on the time-step.

The approach here used for time-marching (known as operator splitting [26], has the disadvantage, when compared with a fully implicit method, of having a narrower stability region. However, this can be enlarged by using multi-stage time-stepping schemes (such as the second order two stage Adams-Bashforth method [23] used in the present work), that are known to have a wider stability region than the single-stage scheme of eq. (41). Moreover, the application of the operator splitting approach does not require the iterative solution of large and sparse linear algebraic systems, making the solution update much cheaper than what an implicit method requires.

The numerical flux in eq. (42) is computed by means of Roe's approximate Riemann solver [27]:

$$\tilde{\mathbf{F}}_n = \frac{1}{2}(\mathbf{F}_{n\,L} + \mathbf{F}_{n\,R}) - \frac{1}{2}\hat{\mathbf{K}}_n|\hat{\mathbf{\Lambda}}_n|\hat{\mathbf{L}}_n(\mathbf{U}_R - \mathbf{U}_L) \tag{44}$$

In eq. (44), the normal physical flux $\mathbf{F}_n$ is computed according to $\mathbf{F}_n = \mathbf{F}n_x + \mathbf{G}n_r$ (with n_x and n_r being the axial and radial components, respectively, of the cell interface outward normal vector), $\mathbf{K}_n$, $\mathbf{L}_n$ and $\mathbf{\Lambda}_n$ are the right and left eigenvector and eigenvalue matrices projected along the cell interface normal direction, while the circumflex accent ($\hat{.}$) is used to denote the Roe-averaged state (computed by using the linearization procedure given in [28]). The meaning of L and R letters is obvious (i.e. they correspond to the i and $i+1$ states, respectively, if the flux is being computed at the interface $i+1/2, j$). Due to the strength of the shocks involved, an appropriate entropy fix is required to avoid numerical instabilities resulting from even-odd decoupling. As prescribed by Quirk [29], pressure disturbances along the shock front are diffused away with targeted application of the HLLE Riemann solver [30]:

$$\tilde{\mathbf{F}}_n = \frac{b^+\mathbf{F}_{n\,R} - b^-\mathbf{F}_{n\,L}}{b^+ - b^-} + \frac{b^+b^-}{b^+ - b^-}(\mathbf{U}_R - \mathbf{U}_L) \tag{45}$$

where the upwind wave speeds b are given by:

$$b^+ = \max(0, V_{n\,R} + a_{\mathrm{R}}, \hat{V}_n + \hat{a}), \tag{46}$$

$$b^- = \min(0, V_{n\,L} - a_{\mathrm{L}}, \hat{V}_n - \hat{a}) \tag{47}$$

In eqs. (46) - (47), V_n is the normal velocity computed as $V_n = u_x n_x + u_r n_r$, while a represents the frozen speed of sound of the mixture.

High-order spatial resolution is achieved by means of parabolic interpolation of the left and right states at the cell interfaces via:

$$\mathbf{U}_L = \frac{1}{6}(2\mathbf{U}_{i-1,j} + 5\mathbf{U}_{i,j} - \mathbf{U}_{i+1,j}) \tag{48}$$

The use of eq. (48) makes the scheme 3rd-order accurate in space [31]. Due to the limiting required for strong nonlinear waves, the reconstructed left and right states must be modified according to:

$$\mathbf{U}_L \leftarrow \mathrm{median}(\mathbf{U}_L,\ \mathbf{U}_{i,j},\ \mathbf{U}^{\mathrm{MP}}) \tag{49}$$

with:

$$\mathbf{U}^{\mathrm{MP}} = \mathbf{U}_{i,j} + \mathrm{minmod}[\mathbf{U}_{i+1,j} - \mathbf{U}_{i,j},\ \alpha(\mathbf{U}_{i,j} - \mathbf{U}_{i-1,j})] \tag{50}$$

being the monotonicity-preserving (MP) limit [32] and $\mathrm{minmod}(a,b) = \frac{1}{2}(\mathrm{sgn}(a)+\mathrm{sgn}(b))\min(\mathrm{abs}(a), \mathrm{abs}(b))$. For the present work, the parameter α has been set to 2. The right state can be easily found from symmetry. Due to the non-linearity of the limiter, the reconstruction is performed on the characteristic variables, requiring a full diagonalization of the governing equations. More details are given in [23].

IV. Computational results

The VC model described in Sec. II has been applied for the computation of the following 2D axisymmetric inviscid flows:

- Supersonic flow through a converging-diverging nozzle,
- Flow over a sphere.

For the first test-case, the nozzle of the NASA Ames EAST facility has been chosen (see Fig. 3), while for the second one a sphere of radius $R = 0.5\,\mathrm{m}$ has been considered. In order to get more physical insight from both simulations, a vibrational temperature T^{v} has been extracted from the vibrational energy level populations by solving the following algebraic non-linear equation:

$$\frac{\sum_{v=0}^{v_{\max}} \tilde{n}_v \tilde{E}_v}{\sum_{v=0}^{v_{\max}} \tilde{n}_v} = \frac{\sum_{v=0}^{v_{\max}} \tilde{E}_v \exp\left(-\frac{\tilde{E}_v}{k_{\mathrm{B}} T^{\mathrm{v}}}\right)}{\sum_{v=0}^{v_{\max}} \exp\left(-\frac{\tilde{E}_v}{k_{\mathrm{B}} T^{\mathrm{v}}}\right)} \tag{51}$$

at each mesh cell.

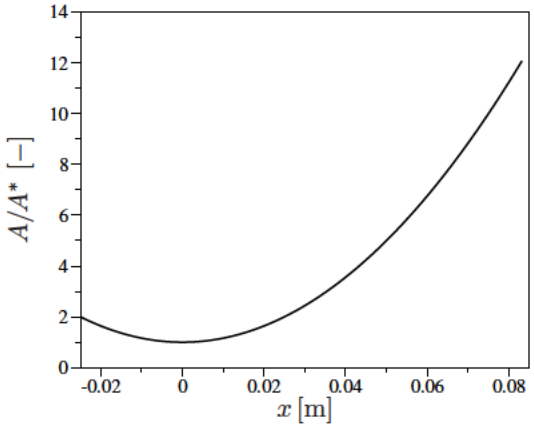

Figure 3. Normalized area distribution of the EAST facility nozzle.

Nozzle flow

The flow is supposed to be in equilibrium at the nozzle inlet. The reservoir total pressure and temperature are, respectively, $p_0 = 100\,\mathrm{atm}$ and $T_0 = 5600\,\mathrm{K}$ and correspond to actual operative conditions of the EAST facility. For the latters, experimental data on vibrational energy level populations (measured by means of Raman spectroscopy) are available [33].

Computations were run by using the 4-block mesh shown in Fig. 4. Each block consists of a 50 x 50 cell grid. In order to assess the solution accuracy on that grid, a convergence study has been performed by doubling the number of cells (for each block) in both radial and axial directions. The solutions obtained by using the original and finer grids did not show appreciable departure from each other, hence justifying the use of the original grid.

Figs. 5 - 6 show the velocity magnitude and temperature (translational and vibrational) fields together with the distribution of the same quantities along the nozzle axis. The flow remains in thermal equilibrium for all the converging part of the nozzle, as can be appreciated from the temperature distribution. Once it crosses the throat, the expansion becomes significant and nonequilibrium effects start to appear. This is caused by the reduction of the flow macroscopic time-scales due to the velocity increase. The translational and vibrational temperatures start deviating from each other, with the latter becoming frozen around $x \simeq 4\,\mathrm{cm}$. Downstream this location, the flow further expands as if the inelastic collisional processes taken into account (see Sec. II) were not occurring.

Figs. 7, show the mass fractions of the N atom, N_2 molecule and the first 9 vibrational levels of the latter. The degree of recombination is quite low. This is due to the fact that the flow in the reservoir is weakly dissociated as an effect of the high and low values of total pressure and temperature, respectively. Despite that, an accurate prediction of the aforementioned quantity is always needed, since a too approximated prediction of the flow outlet conditions can lead to an erroneous interpretation of experimental data acquired in high-enthalpy wind tunnels. From the same figures, one can see that the relative population of the ground state increases, while those of excited states experience depletion.

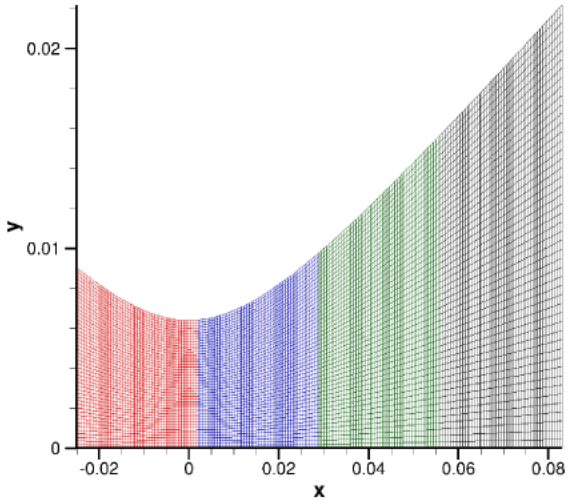

Figure 4. Multi-block mesh used for the EAST facility nozzle (4 blocks — 200 x 50 cells).

This does not mean that the recombination occurs mainly in the ground state. As a matter of fact, the observed behavior of the excited vibrational levels is a consequence of the concurrent action of D_a, D_m processes, leading to the formation of vibrationally excited molecules, and VT_a, VT_m and VV inelastic processes that, as an effect of the cooling the flow is undergoing, lead to an increase of the population of low-lying levels.

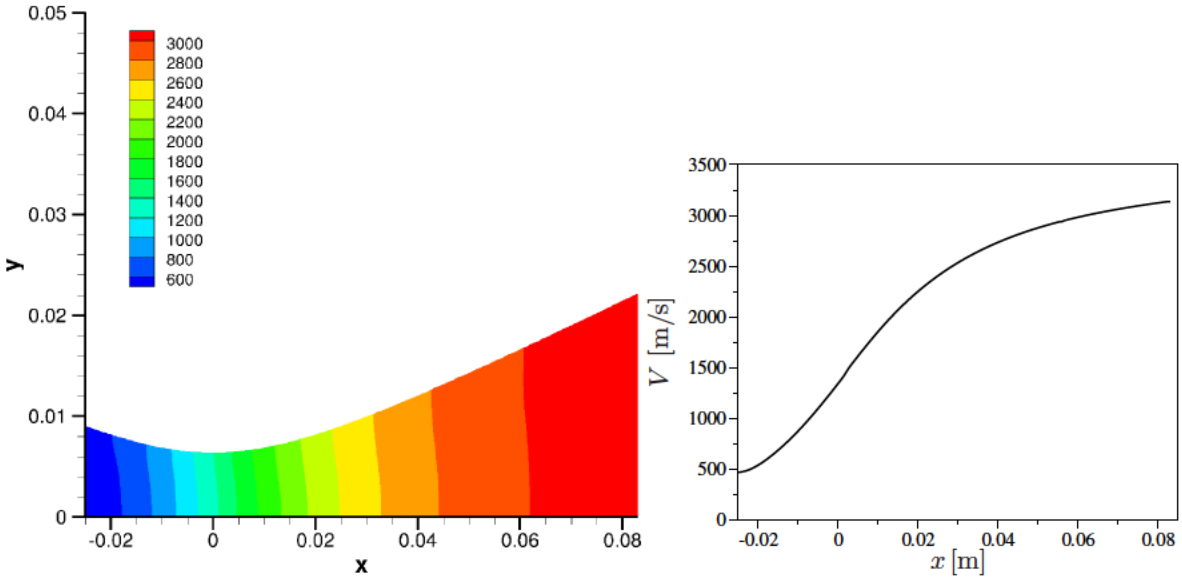

(a) Velocity.

(b) Velocity along nozzle axis.

Figure 5. Velocity field.

The usage of a VC model allows for a detailed investigation of the energy level dynamics. Moreover, since no hypothesis is done on the population distribution, it is possible to check the approximation introduced by classical multi-temperature models (where a Boltzmann distribution at its own temperature is supposed to exist for each species internal degree of freedom). Fig. 8 shows the evolution of the distribution along the nozzle axis. At the inlet, where equilibrium is imposed, all levels lie along a straight line. When the flow begins to expand in the converging portion of the nozzle, the shape of the distribution remains the same. Only the slope changes as an effect of the cooling. A small overpopulation starts to appear (for high-lying levels) at the throat and this becomes more and more pronounced when the flow becomes supersonic. At the outlet, the ground state and low-lying levels are aligned along a straight line (whose slope is proportional to the inverse of the vibrational temperature T^v previously shown) while high-lying levels experience overpopulation. The

latter is an indication that lumping all the levels within a Boltzmann distribution (as done within the context of multi-temperature models) is not possible (for the reservoir conditions adopted here).

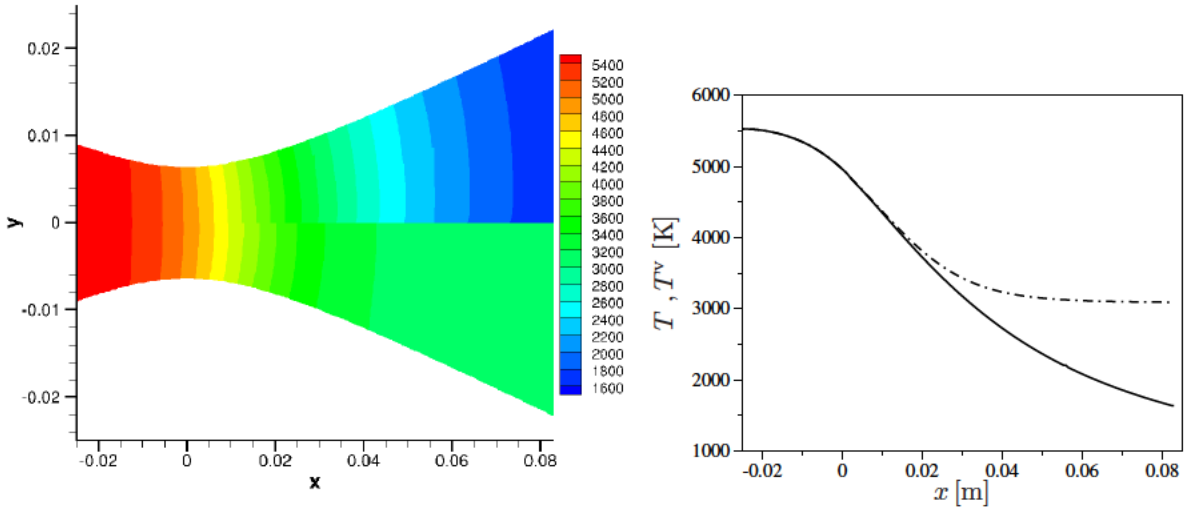

(a) Temperatures (upper part T - lower part T^{v}). (b) Temperatures along nozzle axis (—— T, $-\cdot-$ T^{v}).

Figure 6. Translational and vibrational temperature fields.

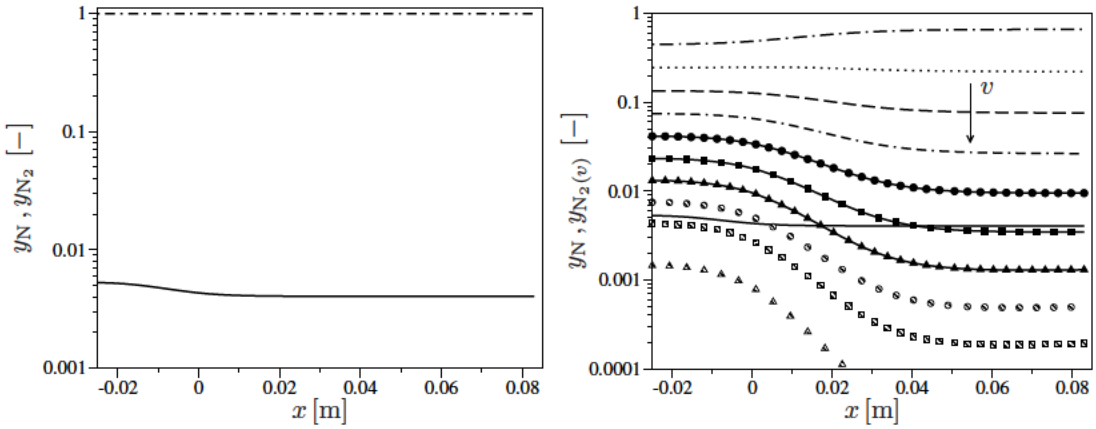

(a) —— N, $-\cdot-$ $\mathrm{N_2}$. (b) —— N, other $\mathrm{N_2}(v)$ (with $v = 0, \ldots, 9$).

Figure 7. Mass fraction evolution along the nozzle axis.

The computed population distributions have been compared against experimental data. These have been obtained by means of Raman spectroscopy [33] at the locations provided in Table 1.

Table 1. Locations of experimental data acquisition.

	1	2	3
x [cm]	-0.6	2.4	5.4

Fig. 9 compares the computed and experimental normalized population distributions for the first 10 vibrational levels of the $\mathrm{N_2}$ molecule. The agreement is excellent for the first location (converging portion of the nozzle), where the flow is close to equilibrium. For the second and third location, the agreement is good for the ground state and the first four excited levels, while discrepancies start to appear for the higher states. In this zone (where measurement errors are more significant), the computational model adopted predicts a Boltzmann distribution at the temperature T^{v}, while an overpopulation appears in experimental

data. The latter could be due to the presence of some nonequilibrium at the nozzle inlet. This possible source of disagreement is totally neglected in the computations, since equilibrium is assumed at nozzle inlet. Moreover, the actual flow in the facility is characterized by the presence of viscous effects and unsteadiness. None of these factors are taken into account within the computational model adopted. In view of that, the comparison between computational and experimental data can be considered satisfactory.

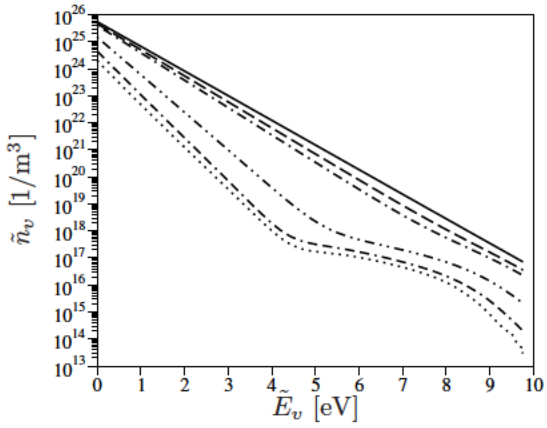

Figure 8. Population evolution along the nozzle axis (—— $x = -2.5\,\text{cm}$, − − − $x = -0.6\,\text{cm}$, −·− $x = 0\,\text{cm}$, −··− $x = 2.4\,\text{cm}$, − − ·− − − $x = 5.4\,\text{cm}$, ···· $x = 8.3\,\text{cm}$).

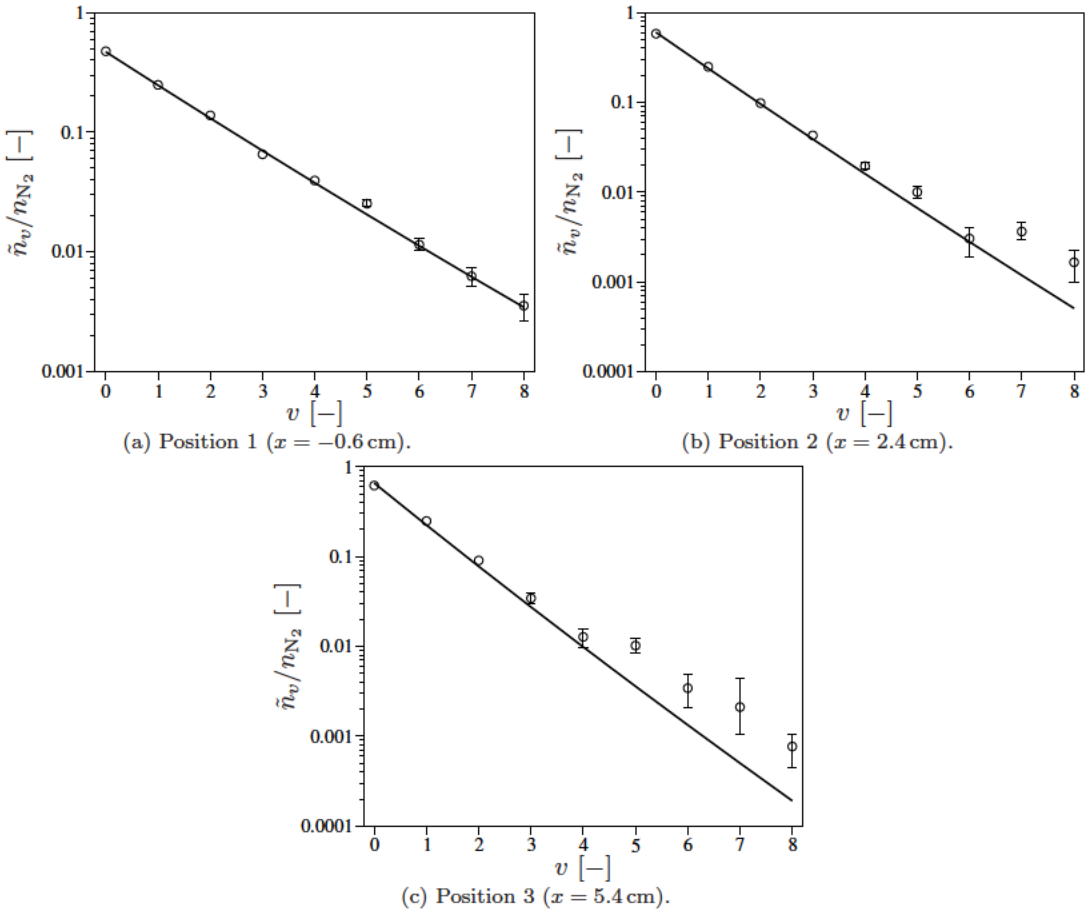

(a) Position 1 ($x = -0.6\,\text{cm}$).

(b) Position 2 ($x = 2.4\,\text{cm}$).

(c) Position 3 ($x = 5.4\,\text{cm}$).

Figure 9. Comparison between computed and experimental normalized vibrational energy level population distributions.

Flow over a sphere

For the computation of the inviscid 2D axisymmetric flow over a sphere, the free-stream conditions provided in Table 2 have been adopted:

Table 2. Free-stream conditions.

p_∞ [Pa]	T_∞ [K]	V_∞ [m/s]
13.3	300	9,000

A 12-block mesh (see Fig. 10), with each block consisting of a 90 x 30 cell grid, has been used.

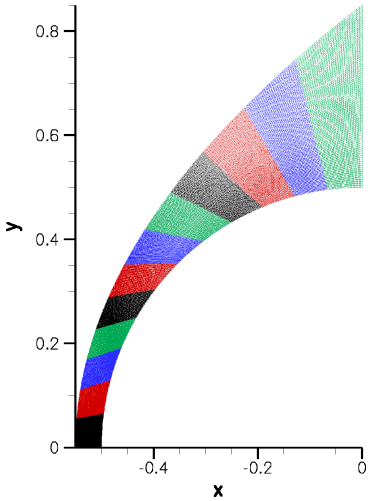

Figure 10. Multi-block mesh used for the sphere (12 blocks — 90 x 360 cells).

Figs. 11 - 12 show the temperature distribution and their evolution along stagnation line, respectively. At the shock location, the vibrational temperature is frozen and maintains its free-station value. Behind the shock, excitation occurs at the beginning mainly through VT_m processes.

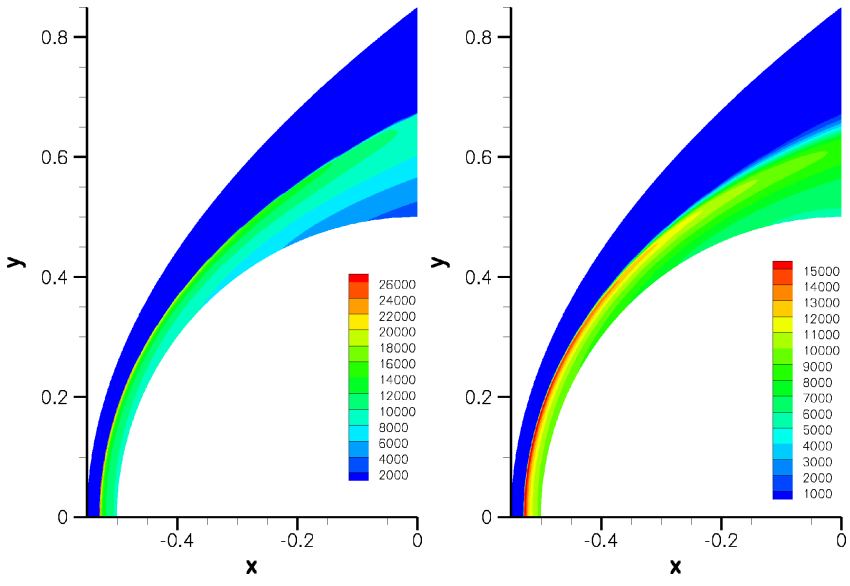

(a) Translational temperature. (b) Vibrational temperature.

Figure 11. Translational and vibrational temperature fields.

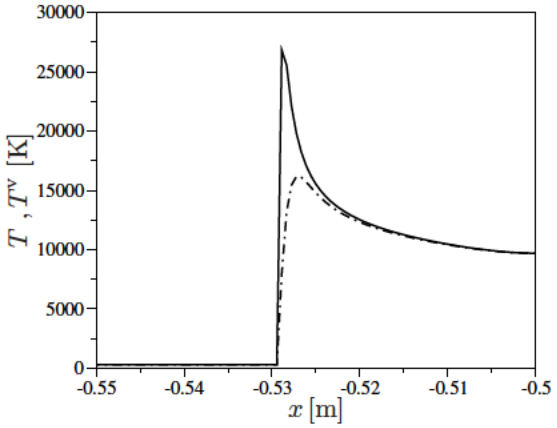

Figure 12. Temperature evolution along the stagnation line.

Once molecules are sufficiently excited, they start to dissociate. In this phase, as soon N is formed because of dissociation, VT_a processes start to occur as well. The collisional excitation leads to an initial increase of the vibrational temperature since medium and high-lying are being populated. On the other hand, the dissociation causes a depletion of the population of vibrational levels and tends to decrease the vibrational temperature value. After an initial stage where molecules are being excited, the dissociation becomes the dominant mechanism and causes the vibrational temperature (as shown in Fig. 12) to reach a maximum and then relax and assume the same value as the translational temperature. Since the flow is inviscid, no boundary layer is present, and the wall temperature assumes the value corresponding to equilibrium conditions downstream the shock. It is interesting to notice that, as opposed to the results obtained by means of multi-temperature models, the vibrational temperature does not become higher than the translational one. The aforementioned behavior is not physical and is due to the use of too approximated formulations for the chemistry-vibration coupling source term [1]. When one uses a VC model (like in the present case), there is no need for this macroscopic source term, since energy levels are treated as pseudo-species and the chemistry-vibration coupling is consistently and intrinsically contained in the rate coefficients for dissociation from all vibrational levels.

The dynamics of the macroscopic dissociation of the N_2 molecule can also be appreciated from Fig. 13, showing the evolution along the stagnation line of the mass fractions of the N atom, N_2 molecule and the first 10 vibrational levels of the latter. These provide a confirmation to what was mentioned before, that is, macroscopic dissociation proceeds through an initial stage of excitation followed by a second phase where dissociation from all vibrational levels becomes the dominant mechanism.

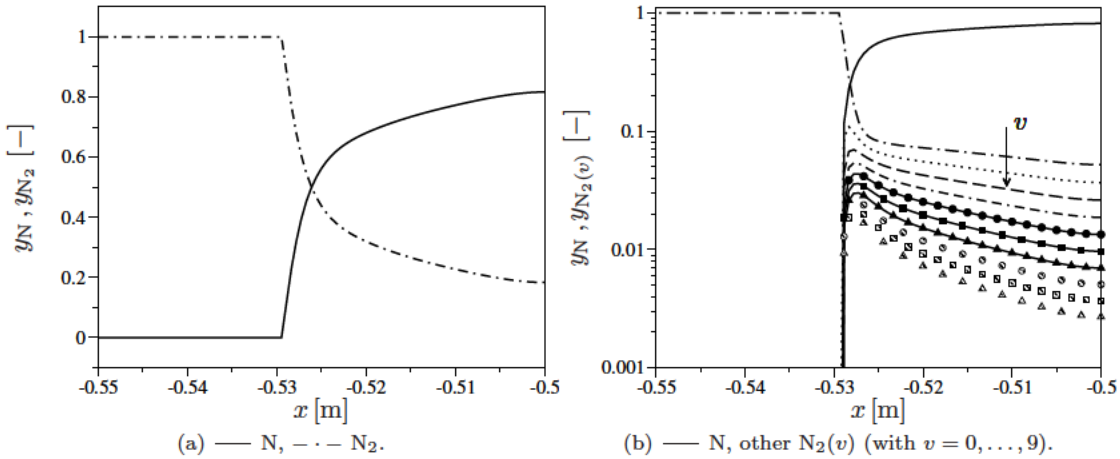

(a) —— N, – · – N_2. (b) —— N, other $N_2(v)$ (with $v = 0, \ldots, 9$).

Figure 13. Mass fraction evolution along the stagnation line.

Fig. 14 shows the evolution of the vibrational energy level population between the shock and wall locations. The initial shape corresponds to a Boltzmann distribution at the free-stream temperature. As soon as the flow crosses the shock, collisional excitation (through single and multi-quantum transitions) starts populating medium and high-lying levels. At this stage the population of vibrational levels strongly deviates from a Boltzmann distribution. After that, N_2 molecules start dissociating and the population of vibrational levels approaches the Boltzmann distribution corresponding to the post-shock equilibrium state. The present analysis, despite the simplicity of the flow field being computed, shows that macroscopic dissociation in a shock layer flow does not occur through a sequence of Boltzmann distributions of vibrational levels.

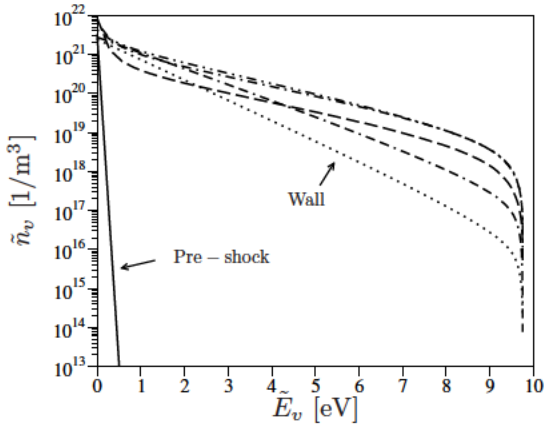

Figure 14. Population evolution along the stagnation line (—— $x = -0.55\,\mathrm{m}$, − − − $x = -0.53\,\mathrm{m}$, − · − $x = -0.525\,\mathrm{m}$, − · · − $x = -0.52\,\mathrm{m}$, − − · − − $x = -0.515\,\mathrm{cm}$, · · · · $x = 0\,\mathrm{m}$).

V. Conclusions

A vibrational collisional model has been developed and applied for investigating nonequilibrium effects in 2D axisymmetric inviscid flows. Applications have considered the supersonic flow through a converging-diverging nozzle (EAST facility of NASA Ames Research Center) and the flow past a sphere. In both cases, the detailed analysis of the vibrational energy level dynamics has shown that, both macroscopic recombination and dissociation do not proceed through a sequence of Boltzmann distributions at their own temperatures (as supposed within the context of multi-temperature models).

The computed vibrational energy level population distributions for the EAST facility nozzle have been compared against experimental data. Despite the simplifying assumption introduced in the modeling phase (inviscid and steady flow) a fair agreement has been observed.

Future work will focus on the implementation of viscous effects and comparison with results obtained by means of multi-temperature models.

Acknowledgements

Research of A. Munafò, M. G. Kapper and T. E. Magin is sponsored by the European Research Council Starting Grant #259354. J.-L. Cambier would like to acknowledge the support of the Air Force Office of Scientific Research, contract #09RZ06COR (Dr. F. Fahroo, Program Manager). The authors would like to thank R. L. Jaffe and D. W. Schwenke at NASA Ames Research Center for providing the rate coefficients of the rovibrational collisional model used in the present work and M. Panesi at University of Texas at Austin for the useful discussions on the formulation of the vibrational collisional model.

References

[1]Park, C., *Nonequilibrium hypersonic aerothermodynamics*, Wiley, New York, 1990.

[2]Park, C., "The limits of two temperature model," AIAA Paper 2010–911, 2010, 48th AIAA Aerospace Sciences Meeting including the new Horizons Forum and Aerospace Exposition, Orlando, Florida.

[3]Jaffe, R. L., Schwenke, D. W., Chaban, G., and Huo, W., "Vibrational and rotational excitation and relaxation of nitrogen

from accurate theoretical calculations," AIAA Paper 2008-1208, 2008, 46th AIAA Aerospace Sciences Meeting and Exhibit, Reno, Nevada.

[4]Jaffe, R. L., Schwenke, D. W., and Chaban, G., "Theoretical analysis of N_2 collisional dissociation and rotation-vibration energy transfer," AIAA Paper 2009–1569, 2009, 47th AIAA Aerospace Sciences Meeting and Exhibit, Orlando, Florida.

[5]Chaban., G., Jaffe, R. L., Schwenke, D. W., and MR., W., "Dissociation cross-sections and rate coefficients for nitrogen from acccurate theoretical calculations," AIAA Paper 2008–1209, 2008, 46th AIAA Aerospace Sciences Meeting.

[6]Schwenke, D. W., "Dissociation cross-sections and rates for nitrogen," *Non-equilibrium Gas Dynamics: from Physical Models to Hypersonic Flights*, Lecture Series, von Karman Institute for Fluid Dynamics, Rhode-Saint-Genèse, Belgium, 2008.

[7]Munafò, A., Panesi, M., Jaffe, R. L., Bourdon, A., and Magin, T., "Mechanism reduction for rovibrational energy excitation and dissociation of molecular nitrogen in hypersonic flows," AIAA Paper 2011-3623, 2011, 11th AIAA/ASME Joint Thermophysics and Heat Transfer Conference, Honolulu, Hawaii.

[8]Magin, T. E., Panesi, M., Bourdon, A., Jaffe., R. L., and Schwenke, D. W., "Coarse-grain model for internal energy excitation and dissociation of molecular nitrogen," *Chemical Physics*, 2011, in press.

[9]Panesi, M., Magin, T. E., Bourdon, A., Bultel, A., and Chazot, O., "Analysis of the Fire II Flight experiment by means of a collisional radiative model," *Journal of Thermophysics and Heat Transfer*, Vol. 23, No. 2, 2009, pp. 236–248.

[10]Cambier, J. L. and Moreau, S., "Simulation of a molecular plasma in collisional-radiative nonequilibrium," AIAA Paper 1993-3196, 1993, 24th AIAA Plasmadynamics & Lasers Conference, Orlando, Florida.

[11]Esposito, F. and Capitelli, M., "Quasi-classical molecular dynamic calculations of vibrationally and rotationally state selected dissociation cross sections: $N + N_2 \rightarrow 3N$," *Chemical Physics Letters*, Vol. 302, No. 1, 1999, pp. 49–54.

[12]Esposito, F. and Capitelli, M., "Quasi-classical dynamics and vibrational kinetics of $N+N_2(v)$ system," *Chemical Physics*, Vol. 257, No. 2, 2000, pp. 193–202.

[13]Colonna, G., Tuttafesta, M., Capitelli, M., and Giordano, D., "Non-Arrhenius NO formation rate in one-dimensional nozzle airflow," *Journal of Thermophysics and Heat Transfer*, Vol. 13, No. 3, 1999, pp. 372–375.

[14]Colonna, G. and Capitelli, M., "Self-consistent model of chemical, vibrational, electron kinetics in nozzle expansion," *Journal of Thermophysics and Heat Transfer*, Vol. 15, No. 3, 2001, pp. 308–316.

[15]Kim, J. G., Kwon, O. J., and Park, C., "Master equation study and nonequilibrium chemical reactions for $H + H_2$ and $He + H_2$," *Journal of Thermophysics and Heat Transfer*, Vol. 23, No. 3, 2009, pp. 443–453.

[16]Jaffe, R. L., "The calculation of high-temperature equilibrium and nonequilibrium speficic heat data for N_2, O_2 and NO," AIAA Paper 1987–1633, 1987, 22nd AIAA Thermophysics Conference, Honolulu, Hawaii.

[17]Magin, T. E., Panesi, M., Bourdon, A., Jaffe, R. L., and Schwenke, D. W., "Internal energy excitation and dissociation of molecular nitrogen in a compressing flow," AIAA Paper 2009–3837, 2009, 41st AIAA Thermophysics Conference, San Antonio, Texas.

[18]Chernyi, G. . G., Losev, S. A., Macheret, S. O., and Potapkin, B. V., *Physical and chemical processes in gas dynamics: cross sections and rate constants for physical and chemical processes*, American Institute for Aeronautic and Astronautics, 2002.

[19]Billing, G. D. and Fisher, E. R., "VV and VT rate coefficients in N_2 by a quantum-classical mode," *Chemical Physics*, Vol. 43, No. 3, 1979, pp. 395–401.

[20]Herzberg, G., *Molecular spectra and molecular structure*, D. Van Nostrand, Inc., New York, 1963.

[21]Colonna, G., Pietanza, L. D., and Capitelli, M., "Macroscopic rates with vibrational nonequilibrium for N_2 dissociation," AIAA Paper 2007–4554, 2007, 39th AIAA Thermophysics Conference, Miami, Florida.

[22]Capitelli, M., Ferreira, C. M., Gordiets, B. F., and Osipov, A. I., *Plasma kinetics in atmospheric gases*, Springer, 2000.

[23]Kapper, M. G., *A high-order transport scheme for collisional-radiative and nonequilibrium plasma*, Ph.D. thesis, The Ohio State University, 2009.

[24]Kapper, M. G. and Cambier, J., "Ionizing shocks in Argon. Part I: Collisional-radiative model and steady-state structure," *Journal of Applied Physics*, Vol. 109, No. 11, 2011, pp. 113308.

[25]Kapper, M. G. and Cambier, J., "Ionizing shocks in Argon. Part II: Transient and multi-dimensional effects," *Journal of Applied Physics*, Vol. 109, No. 11, 2011, pp. 113309.

[26]Hirsch, C., *Numerical computation of internal and external flows*, John Wiley and Sons, Chichester, UK, 1988.

[27]Roe, P. L., "Approximate Riemann solvers, parameter vectors and difference schemes," *Journal of Computational Physics*, Vol. 43, No. 2, 1981, pp. 357–372.

[28]Prabhu, R. K., "An implementation of a chemical and thermal nonequilibrium flow solver on unstructured meshes and application to blunt bodies:s," NASA CR 194867, 1994.

[29]Quirk, J. J., "A contribution to the great Riemann solver debate," *International Journal for Numerical Methods in Fluids*, Vol. 18, No. 6, 1994, pp. 555–574.

[30]Einfeldt, B., Munz, C. D., Roe, P. L., and Sjogreen, B., "On Godunov-type methods near low densities," *Journal of Computational Physics*, Vol. 92, No. 2, 1991, pp. 273–295.

[31]van Leer, B., "Towards the ultimate conservative difference scheme (IV). A new numerical approach to numerical convection," *Journal of Computational Physics*, Vol. 23, No. 3, 1977, pp. 276–299.

[32]Suresh, A. and Huynh, H. T., "Accurate monotonicity-preserving schemes with Runge-Kutta time stepping," *Journal of Computational Physics*, Vol. 136, No. 1, 1997, pp. 83–99.

[33]Sharma, S. P., Ruffin, M. R., Gillespie, W. D., and Meyer, S. A., "Vibrational relaxation measurements in an expanding flow using spontaneous Raman scattering," *Journal of Thermophysics and Heat Transfer*, Vol. 7, No. 4, 1993, pp. 697–703.